



# Simultaneous increase of conductivity, active sites and structural strain by nitrogen injection for high-yield CO<sub>2</sub> electro-hydrogenation to liquid fuel

Yi Li<sup>a</sup>, Guoqiang Shi<sup>a</sup>, Tao Chen<sup>c</sup>, Lin Zhu<sup>a</sup>, Dengfeng Yu<sup>b</sup>, Ye Sun<sup>b</sup>, Flemming Besenbacher<sup>d</sup>, Miao Yu<sup>a,\*</sup>

<sup>a</sup> State Key Laboratory of Urban Water Resource and Environment, School of Chemistry and Chemical Engineering, Harbin Institute of Technology, Harbin 150000, China

<sup>b</sup> Condensed Matter Science and Technology Institute, School of Instrumentation Science and Engineering, Harbin Institute of Technology, Harbin 150000, China

<sup>c</sup> State Key Laboratory of Environment-friendly Energy Materials, Southwest University of Science and Technology, Mianyang, Sichuan 621010, China

<sup>d</sup> Interdisciplinary Nanoscience Center (iNANO), Aarhus University, Aarhus 8000, Denmark

## ARTICLE INFO

### Keywords:

CO<sub>2</sub> electrohydrogenation  
Liquid fuel  
Conductivity  
Nitrogen-injection  
CuSe nanosheets

## ABSTRACT

Electrocatalytic hydrogenation of CO<sub>2</sub> has become particularly promising to address the grand issues of global warming and energy crisis. Herein, we report simultaneous increase of conductivity, active sites and structural strain of copper selenide nanosheets by nitrogen (N)-injection (N-CuSe), resulting in significant improvement in CO<sub>2</sub> electroreduction. At the applied potential of  $-1.1$  V vs. reversible hydrogen electrode in CO<sub>2</sub>-saturated 0.5 mol L<sup>-1</sup> KHCO<sub>3</sub>, the N-CuSe delivers a current density of  $\sim 46.7$  mA cm<sup>-2</sup>, 3.1-folds as that of the pristine CuSe. A high production yield of liquid products containing formate ( $\sim 22.1$  mg h<sup>-1</sup> cm<sup>-2</sup>), acetate ( $\sim 1.2$  mg h<sup>-1</sup> cm<sup>-2</sup>) and ethanol ( $\sim 1.0$  mg h<sup>-1</sup> cm<sup>-2</sup>) is achieved by N-CuSe, which is over 11-folds as that produced by the pristine CuSe. Such a facile strategy simultaneously enhancing conductivity, active sites and structural strain holds great promise on promoting catalysts for a big variety of reactions, not limited to CO<sub>2</sub> electroreduction.

## 1. Introduction

As an effective strategy for carbon neutrality, electrocatalytic hydrogenation of carbon dioxide (CO<sub>2</sub>) to produce high value-added fuels and carbonaceous feedstock has sparked enormous interest in recent years [1–4]. Nevertheless, due to the symmetrical linear structure and stable C=O bonding of CO<sub>2</sub> molecules, inefficient conversion from CO<sub>2</sub> to the target products remains the bottleneck for CO<sub>2</sub> hydrogenation [5]. To boost the conversion efficiency, considerable efforts have been devoted to the design and manufacture of high-performance electrocatalysts [6–9]. Despite the major success achieved from the developed catalysts, the limited production yield and current density upon CO<sub>2</sub> conversion are the major challenges for CO<sub>2</sub> electroreduction.

To accelerate the electrocatalytic rate and yield in CO<sub>2</sub> reduction reaction (CO<sub>2</sub>RR), various strategies have been proposed to design advanced electrocatalysts [10–12]. Like in most catalytic reactions, the establishment of active sites (e.g. heteroatom doping, creating vacancies/grain boundaries) is an effective route to induce local accumulation of electrons/holes hence promote the catalytic rate/path and adsorption capacity in CO<sub>2</sub>RR [13–17]. Enhancement of catalysts' conductivity has

been acknowledged to be another effective approach [18]: by introducing a defect level in the band structure [19], utilizing the electron-cloud spin splitting [20], or triggering structural re-arrangement/phase transition [21,22], the increased charge transport capability can largely benefit the current density in electrocatalysis towards a bumper harvest of carbon products from CO<sub>2</sub>RR. In addition, engineering structural strain also holds great promise on upgrading the electrocatalytic capability [23,24]. Theoretical studies suggested that surface strain as low as 1% can already change the adsorption energy of reaction intermediates significantly [25,26]. So far, facile approaches that simultaneously address the active sites, conductivity and structural strain of electrocatalysts remain scarce and highly desirable.

Herein, we report simultaneous enhancement of conductivity, active sites and structural strain of cubic-phase copper selenide (CuSe) via nitrogen (N) injection for high-yield CO<sub>2</sub> electrohydrogenation. The strategy was evaluated by density functional theory (DFT) calculations prior to synthesis: the introduction of N to the parent catalyst was found to effectively modulate its inherent electronic structure to be more metallic, with abundant delocalized electrons accumulated around the injected N atoms, meanwhile induce a small structural distortion around

\* Corresponding author.

E-mail addresses: [sunye@hit.edu.cn](mailto:sunye@hit.edu.cn) (Y. Sun), [miaoyu\\_che@hit.edu.cn](mailto:miaoyu_che@hit.edu.cn) (M. Yu).

<https://doi.org/10.1016/j.apcatb.2022.121080>

Received 2 October 2021; Received in revised form 3 December 2021; Accepted 4 January 2022

Available online 6 January 2022

0926-3373/© 2022 Elsevier B.V. All rights reserved.

N. We then engineered ultrathin CuSe nanosheets with N atoms deliberately injected in their lattice (N-CuSe). Thanks to the enhanced conductivity, local charge re-distribution and structural strain induced by N injection, significant improvement in the electrocatalytic activity for CO<sub>2</sub>RR has been achieved. Typically, at the applied potential of  $-1.1$  V vs. reversible hydrogen electrode (RHE) in CO<sub>2</sub>-saturated  $0.5 \text{ mol L}^{-1}$  KHCO<sub>3</sub> aqueous solution, the N-CuSe delivered a current density of CO<sub>2</sub>RR as high as  $\sim 46.7 \text{ mA cm}^{-2}$ , 3.1-folds as that of the pristine CuSe. The selectivity of carbonous products increased from  $\sim 39.8\%$  for the pristine CuSe to  $\sim 81.4\%$  for N-CuSe, and the proportion of liquid products increased from  $\sim 15.4\%$  to  $\sim 78.9\%$ . The products converted by N-CuSe contained 23.5% C<sub>2</sub> products (acetate and ethanol), which were not detected in the case of CuSe. Especially, a remarkably high production yield of liquid products containing  $\sim 22.1 \text{ mg}$  of formate (over 11-folds as that produced by the parent catalyst),  $\sim 1.2 \text{ mg}$  of acetate, and  $\sim 1.0 \text{ mg}$  of ethanol [per hour and per unit area of the electrode ( $\text{cm}^2$ )] was achieved by N-CuSe. This work not only proposes a powerful new catalyst, but also opens up a rapid route to boost the yield and current density for CO<sub>2</sub> electroreduction efficiently.

## 2. Experimental section

### 2.1. Calculation methods

The Vienna *ab initio* simulation package (VASP) [27,28] was used to carry out the DFT calculations. The Perdew-Burke-Ernzerhof (PBE) exchange-correlation density functional [29] and projector augmented wave (PAW) potentials were used to describe the interaction of ionic cores and electrons. The force convergence criterion used for the geometry relaxation was  $0.02 \text{ eV } \text{\AA}^{-1}$ . For the density of states (DOS) calculations, a plane-wave cutoff energy of 480 eV and Gamma k-point mesh of  $19 \times 19 \times 19$  in the Brillouin zone were sampled.

### 2.2. Synthesis of CuSe nanosheets

The hexagonal-phase CuSe nanosheets were fabricated according to the reported method with minor adjustments [30]. Typically, NaOH (50 mmol) was added into a round-bottom flask (50 mL) containing deionized water (20 mL) to form a clear solution by magnetic agitation for 10 min. After adding Se powder (1 mmol), the solution was heated to  $90^\circ\text{C}$  in oil bath for 30 min until it turned to uniform dark red solution. Subsequently, Cu(NO<sub>3</sub>)<sub>2</sub>·3 H<sub>2</sub>O ethanol solution ( $0.1 \text{ mol L}^{-1}$ , 5 mL) was injected immediately into the flask. Five minutes later, the product was collected by centrifugation at 5000 rpm for 5 min and washed for several times, and finally dried in vacuum overnight.

### 2.3. N-injection to the CuSe nanosheets

The as-prepared hexagonal-phase CuSe nanosheets (100 mg) was placed in a quartz tube and heated to  $400^\circ\text{C}$  at a rate of  $10^\circ\text{C min}^{-1}$  under a mixed gas flow of 10%NH<sub>3</sub>/90%Ar. After reacted at  $400^\circ\text{C}$  for different duration (1–5 h), the products (N-CuSe- $\alpha$ ,  $\alpha = 1, 2, 3, 5$ ) were cooled to the ambient temperature. In the same way, hexagonal-phase CuSe nanosheets were heated in a quartz tube at  $400^\circ\text{C}$  but in pure N<sub>2</sub> atmosphere, the pristine CuSe sample was produced.

### 2.4. Characterization

The morphology and structure of the samples were characterized by field emission scanning electron microscope (SEM, ZEISS SUPRA55), high-resolution field emission transmission electron microscopy (TEM, Tecnai G2 F30), and atomic force microscope (AFM, Bruker Multi-Mode8). The composition was analyzed by X-ray diffraction (XRD, PANalytical X'Pert Pro) and X-ray photoelectron spectroscopy (XPS, Thermo Fisher Scientific, ESCALAB250Xi). The Cu K-edge X-ray absorption fine structure spectroscopy (XAFS) was measured at the

National Synchrotron Radiation Laboratory (NSRL) and the Beijing Synchrotron Radiation Factory (BSRF). The Raman spectra was collected using Alpha 300 R Laser Raman Spectroscopy (Raman, Horiba HR). The liquid products were quantified by <sup>1</sup>NMR (Bruker ADVANCEIII 400 MHz). The gas products were monitored by gas chromatography analyzer (TECHCOMP GC-7900).

### 2.5. Evaluation of the electrocatalytic performance

To prepare the working electrode, catalyst (1 mg), active carbon (4 mg), and Nafion solution (5 wt%, 30  $\mu\text{L}$ ) were added in ethanol (2 mL) to form a homogeneous ink via ultrasonic for 1 h. The ink (1 mL) was then spread on  $1 \times 1 \text{ cm}^2$  carbon paper and dried naturally to obtain the working electrode. The test of CO<sub>2</sub> electrochemical reduction was conducted by using an electrochemical station (CHI660E) with three-electrode system in an H-cell (separated by Nafion 115) containing KHCO<sub>3</sub> electrolyte ( $0.5 \text{ mol L}^{-1}$ , 80 mL) under ambient conditions. Ag/AgCl electrode (in saturated KCl solution) and platinum electrode were chosen as the reference and counter electrodes, respectively. All applied potentials against the Ag/AgCl electrode were converted to that against the reversible hydrogen electrode (RHE) according to:  $E \text{ (vs. RHE)} = E \text{ (vs. Ag/AgCl)} + 0.21 \text{ V} + 0.0591 \times \text{pH}$ .

## 3. Results and discussion

### 3.1. DFT calculations for the N-injected CuSe nanosheet

Due to the moderate affinity with the intermediates (e.g. \*COOH, \*CHO, etc.), Cu-based catalysts (e.g. copper oxides/sulfides) have been widely employed in CO<sub>2</sub> electroreduction [3]. Copper selenide is a typical *p*-type semiconductor with high stability, having demonstrated great promise in thermoelectric conversion [31,32], catalysis of oxygen evolution reaction [33] and plasma techniques [34], but scarcely been applied in CO<sub>2</sub>RR [35]. Promisingly, the nonstoichiometric phases Cu<sub>2-x</sub>Se showed excellent electrochemical properties [32]; the Se atoms at the edges of metal selenides can easily adsorb the intermediates to enhance the CO<sub>2</sub>RR activity [36]; the combination of electron-rich sites (Se atoms) and electron-deficient sites (Cu atoms) was suggested to benefit the formation of carbonaceous products synergistically [37]. N-doping is a facile method to improve the current density in electrocatalyzed CO<sub>2</sub>RR [38], whilst its influence on the electronic structure of the parent catalysts remains vague.

We first investigated the effect of N injection on the electronic structure of CuSe using DFT calculations. As shown in Fig. 1a, the parent catalyst we used was a two-dimensional cubic-phase CuSe sheet containing five atomic-layers (three layers of Se and two layers of Cu between two adjacent Se layers) with a  $3 \times 3$  unit cell. One N atom was introduced into each unit cell and placed in the cell center. According to the calculated DOS, the introduction of N can modify the CuSe from a narrow-bandgap semiconductor to a semi-metal (Fig. 1b): the pristine CuSe showed a narrow gap between the bottom of the conduction band and the top of the valence band (enlarged in the red square), whilst a defect energy level was induced near the Fermi level for N-CuSe, which significantly increased the DOS and eliminated the bandgap.

Next, we analyzed the contribution of each element's orbitals to the total DOS (Fig. 1c). It was found that the *p* orbital of N and Se primarily accounted for the increased DOS near the Fermi level of N-CuSe; the overlap of the *p* orbital of N with the *d* orbital of Cu and the *p* orbital of Se (marked by the grey area) suggested the N – Cu and N – Cu bonding in N-CuSe. To classify the bonding type, electron localization function (ELF) mapping of N-CuSe was calculated (Fig. 1d), where the color represented the electron localization status. The ELF values of the regions between N and Cu and those between N and Se were of 0.2–0.3 (charge delocalization), suggesting weak metallic bonding of N with Cu and Se [39]. The charge accumulation and depletion were then analyzed by the charge density difference plot (Fig. 1e), showing abundant

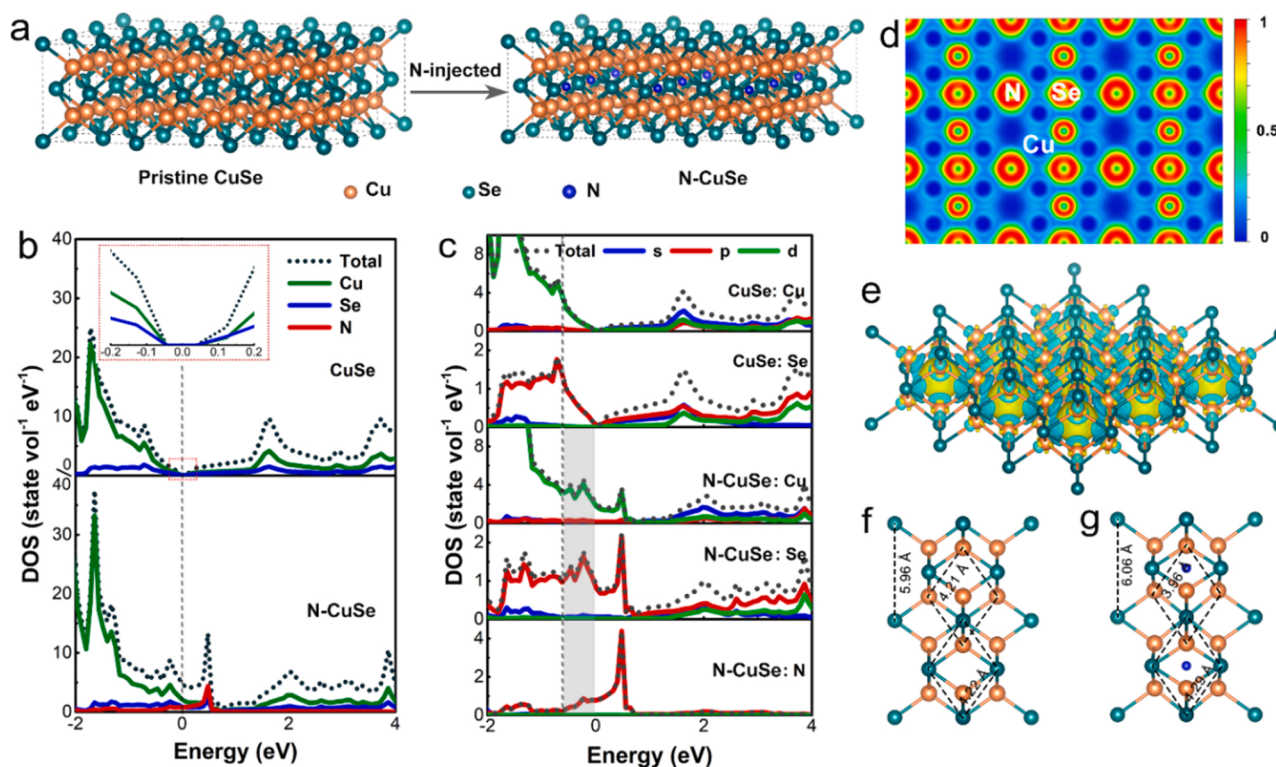


**Fig. 1.** The effect of N injection on the electronic structure of CuSe based on DFT calculations. (a) Fully-relaxed structural model of the pristine and N-injected CuSe nanosheet (N-CuSe), where Cu, Se and N atoms are in golden brown, aqua and blue, respectively. (b) The calculated total and partial DOS of CuSe and N-CuSe, where the Fermi level is pointed out by the vertical dash line. (c) The distribution of DOS contributed from the electrons in the different orbitals of Cu, Se, and N atoms. (d) ELF mapping and (e) plot of charge density difference of N-CuSe. In e, the isosurface value is  $0.002 \text{ e } \text{\AA}^{-3}$ ; the cyan and yellow-green colors indicate charge depletion and accumulation, respectively. DFT optimized structural model of two unit cells of (f) the pristine CuSe and (g) N-CuSe, showing the lattice variation.

electrons accumulated around the N sites that donated from the Cu atoms. Moreover, the interlayer spacing of N-CuSe was enlarged compared with the pristine CuSe, with a small contraction of Cu atoms towards the N atoms and a small expansion of Se atoms moved away (Fig. 1f and g). These results indicate that N injection can increase conductivity meanwhile generate active sites and structural strain for CuSe.

### 3.2. Synthesis and characterization of the N-injected CuSe nanosheets

We subsequently fabricated the pristine and N-injected CuSe nanosheets. As shown in Fig. 2a, with Se powder and  $\text{Cu}(\text{NO}_3)_2 \cdot 3 \text{H}_2\text{O}$  as precursors, hexagonal CuSe nanosheets were first self-assembled under alkaline conditions (Fig. S1) and then annealed at  $400^\circ\text{C}$  in  $\text{N}_2$  atmosphere (Pristine CuSe). Upon N-injection, the hexagonal nanosheets were heated to  $400^\circ\text{C}$  and reacted under  $\text{NH}_3/\text{Ar}$  flow for various duration. Under the given conditions,  $\text{NH}_3$  molecule can first adsorb on the surface of the parent material, and then the adsorbed  $\text{NH}_3$  molecules are dehydrogenated so that the N atoms diffuse into the lattice of the sample [40,41]. The obtained products were denoted as N-CuSe- $\alpha$ , where  $\alpha$  represented the reaction hours. Note that both the pristine and N-injected samples converted from hexagonal phase to cubic phase during annealing. The cubic phase is preferred as it has a higher stability.

Seen from the SEM images, the morphology of N-CuSe-3 was not varied significantly compared with that of the pristine CuSe (Fig. S2). The TEM image further revealed the lamellar structural nature of N-CuSe-3, where the nearly transparent sheets indicated their ultrathin thickness (Fig. 2b). High-resolution TEM (HRTEM) image of N-CuSe-3 exhibited that the interplanar spacing of the lattice along the two close-packed directions was  $\sim 0.20 \text{ nm}$  (Fig. 2c), attributed to (220) planes of cubic-phase CuSe [35]. The energy dispersive X-ray (EDX) elemental

mapping images of N-CuSe-3 showed even distribution of Cu, Se, and N elements over the entire nanosheets (Fig. 2d). Deduced from the AFM image (Fig. 2e), the typical thickness of N-CuSe-3 nanosheets was  $\sim 4.5 \text{ nm}$ . XRD patterns of N-CuSe-3 and the pristine nanosheets (Fig. 2f) were both well indexed to the non-stoichiometric cubic phase of copper selenide, i.e.  $\text{Cu}_{2-x}\text{Se}$  (JCPDS No. 06-0680). Consistent with the HRTEM results, the (220) diffraction peak was the primary one, suggesting that (220) planes were dominant for the lateral structure of the nanosheets. The diffraction peaks of N-CuSe-3 shifted to lower angles relative to those of the pristine sample, indicating lattice expansion induced by N insertion and consistent with the DFT calculation results. The structural distortion was associated with the content of N doping. Upon excessive reaction with  $\text{NH}_3$ , N-CuSe-5 presented umangite structure similar to that  $\text{Cu}_3\text{Se}_2$  (Fig. S3).

The chemical structure of the samples was further explored by XPS, Raman spectroscopy, X-ray absorption near-edge structure (XANES) and extended X-ray absorption fine structure (EXAFS) analysis. The Cu  $2p$  XP spectrum of N-CuSe-3 (Fig. 3a) showed two components for Cu  $2p_{3/2}$  and two for  $2p_{1/2}$ , where the peaks located at  $932.6$  and  $952.4 \text{ eV}$  are associated with Cu(I) and those at  $934.7$  and  $954.8 \text{ eV}$  are assigned to Cu(II), respectively [42]. Consistent with the XRD and HRTEM results, the combination of Cu(I) and Cu(II) further indicated the non-stoichiometry of the nanosheets as  $\text{Cu}_{2-x}\text{Se}$ , where  $x$  was estimated to be  $\sim 0.28$  based on the atomic percentage (i.e.  $\text{Cu}_{1.72}\text{Se}$ ). The nanosheets' names maintained as 'CuSe' for simplification. Compared with that in the pristine sample, the intensity of the Cu(II) component in N-CuSe-3 was reduced, which is attributed to the partial reduction of Cu(II) when reacted with  $\text{NH}_3$  [43]. Moreover, a red shift of these peaks was observed for N-CuSe-3; this is attributed to the increased electron donation of Cu when the more electronegative N atoms (than Se) were introduced. The Se  $3d$  XP spectra of both samples (Fig. 3b) presented two peaks at  $53.9$  and  $54.7 \text{ eV}$  for  $3d_{5/2}$  and  $3d_{3/2}$ , respectively, suggesting the existence of

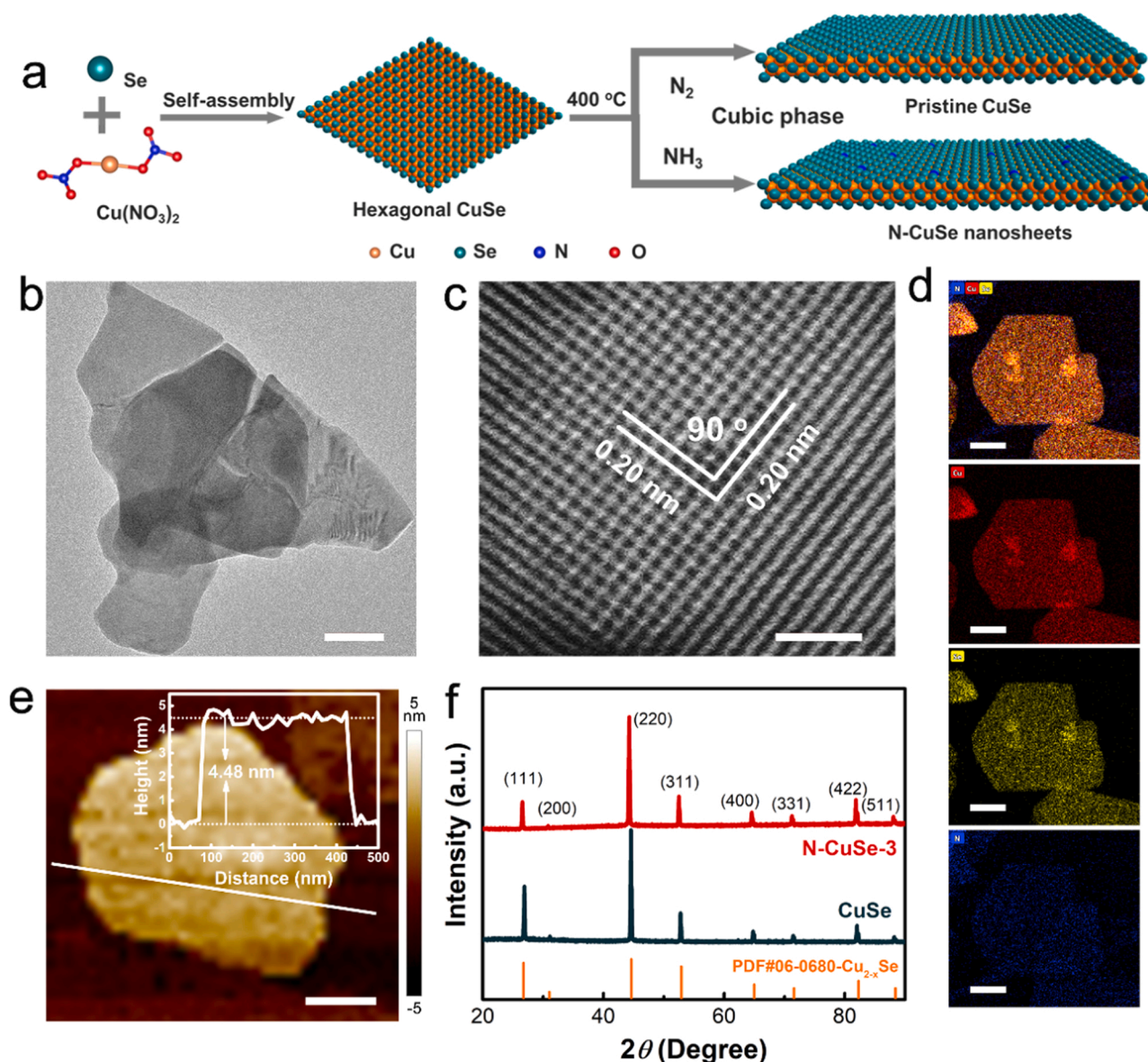


**Fig. 2.** Morphology and structure of the CuSe nanosheets. (a) Schematic illustration for synthesis of the pristine and N-injected CuSe nanosheets. (b) TEM image, (c) HRTEM image, (d) STEM-EDX elemental mapping images, and (e) AFM image of N-CuSe-3 nanosheets. The scale bars in b–e are 100 nm, 1 nm, 200 nm and 100 nm, respectively. The mapping of Cu, Se, N element is in red, yellow and blue, respectively.

$\text{Se}^{2-}$  [44]. XPS survey (Fig. S4) confirmed the successful injection of N atoms, showing that the N content increased gradually with the reaction hours with  $\text{NH}_3$ . The N 1s XP spectra (Fig. 3c) revealed ~12% content of N in N-CuSe-3. The peaks at ~398.4 and 400.6 eV were attributed to the interstitial N [45] and surface-adsorbed N-H/ $\text{NH}_3$  [46], respectively.

In the Raman spectrum of N-CuSe-3 (Fig. 3d), the strong vibration at  $263\text{ cm}^{-1}$  was characteristic of Cu–Se bonding and the weak signal at  $201\text{ cm}^{-1}$  was attributed to the transverse optical mode of CuSe [47]. Relative to the pristine sample, the shift of  $\sim 6\text{ cm}^{-1}$  and the narrower full width at half maximum of the primary peak implied that the injected N caused lattice distortion and internal stress [48]. In addition, the white line of normalized XANES spectrum at the Cu *k*-edge of N-CuSe-3 (inset of Fig. 3e) blue-shifted relative to that of the pristine CuSe and Cu foil (standard reference), further confirming that the valence of Cu was reduced by N injection [49]. Fourier transform EXAFS analysis of N-CuSe-3 (Fig. 3f) displayed the primary Cu–Se peak at  $\sim 2.12\text{ \AA}$ , which was higher than that of the pristine CuSe but lower than that of Cu foil. This is attributed to the lattice expansion hence lengthened Cu–Se

bonds caused by the presence of N atoms.

### 3.3. CO<sub>2</sub>RR performance of as-synthesized catalysts

To evaluate the CO<sub>2</sub>RR capability of N-CuSe, we first investigated the potentiodynamic electrochemical behavior of the nanosheets in an H-cell containing 80 mL of CO<sub>2</sub>-saturated 0.5 mol L<sup>−1</sup> KHCO<sub>3</sub> solution. The linear sweep voltammetry (LSV) curve of N-CuSe-3 (Fig. 4a) showed a cathode peak at  $-1.1\text{ V}$  vs. RHE in CO<sub>2</sub>-saturated solution, whilst no peak was observed for the pristine CuSe in CO<sub>2</sub>-saturated solution or N-CuSe-3 in N<sub>2</sub>-saturated KHCO<sub>3</sub>; the cathode peak was then attributed to the CO<sub>2</sub> reduction induced by N-CuSe-3 [50]. Moreover, the current density was significantly varied by the N-injection hours (Fig. S5): N-CuSe-3 nanosheets exhibited the highest current density ( $49\text{ mA cm}^{-2}$  at  $-1.1\text{ V}$  vs. RHE) among all N-CuSe- $\alpha$  ( $\alpha = 1, 2, 3, 5$ ), which was evidently higher than the case of the pristine CuSe ( $13\text{ mA cm}^{-2}$ ). The boosted current density was closely associated with the semi-metallic nature and charge re-distribution of CuSe induced by the presence of N atoms, indicating that the optimum N-injected sample was N-CuSe-3.

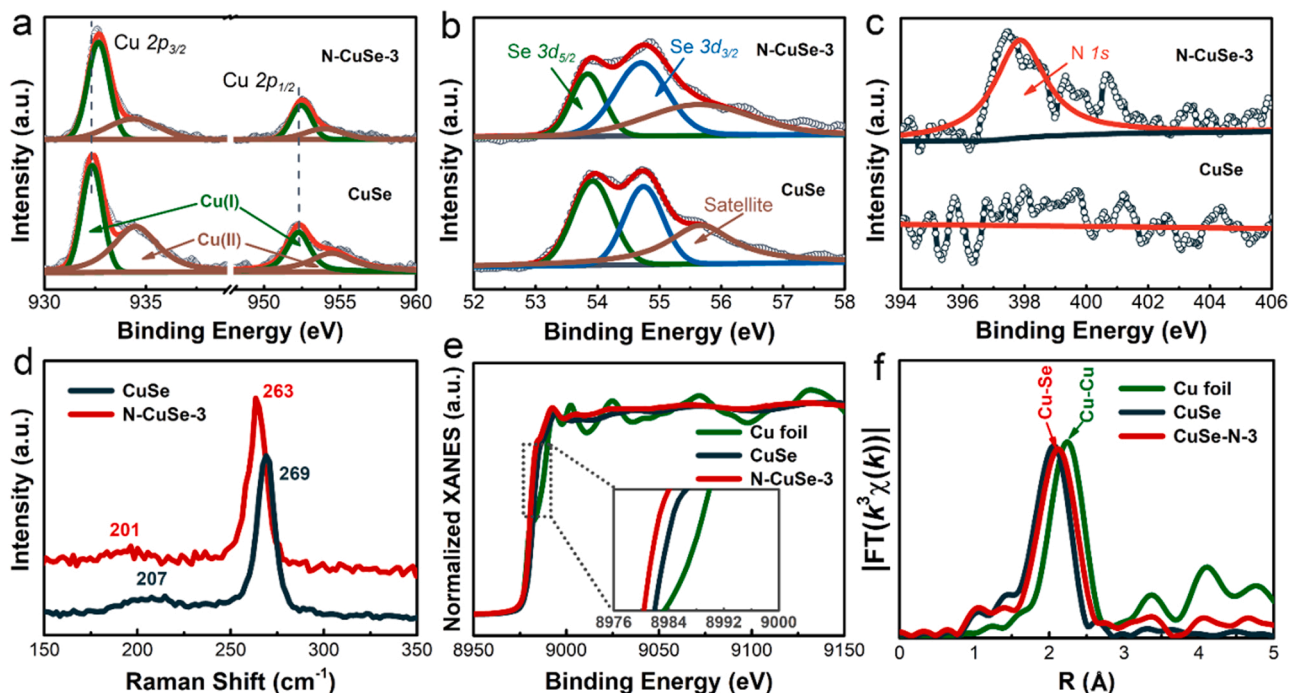


**Fig. 3.** Chemical structure analysis of the N-CuSe samples. (a) High resolution Cu 2p, (b) Se 3d, and (c) N 1s XP spectra, (d) Raman spectra of N-CuSe-3 and the pristine CuSe nanosheets. (e) Cu K-edge XANES and (f)  $K^3$ -weighted  $\chi(k)$  function of Fourier transform EXAFS spectra of N-CuSe-3, CuSe and Cu foil.

In addition, the chronoamperometry curves of all N-CuSe- $\alpha$  samples presented steady current densities at different applied potentials (Fig. S6), suggesting their good electrochemical stability during CO<sub>2</sub>RR.

Consistent with the LSV curves, the geometrical current density ( $j_{total}$ , Fig. 4b) increased with the applied potentials and N-CuSe-3 delivered the highest current density ( $46.7 \text{ mA cm}^{-2}$  at  $-1.1 \text{ V}$  vs. RHE), which was 3.1 folds as that of the pristine CuSe ( $14.9 \text{ mA cm}^{-2}$ ). Moreover, N-CuSe-3 exhibited a largely enhanced partial current density for carbonaceous products ( $j_{C-products}$  of  $37.6 \text{ mA cm}^{-2}$ , Fig. 4c) and for liquid products ( $j_{L-products}$  of  $36.7 \text{ mA cm}^{-2}$ , Fig. 4d), which were 6.2 and 16-times higher than that of the pristine CuSe, respectively. At all the applied potentials, N-CuSe-3 brought on the current density superior to the other samples, suggesting its considerable electrocatalytic promise for CO<sub>2</sub>RR.

The carbonaceous products catalyzed by N-CuSe- $\alpha$  and the pristine CuSe were quantified by nuclear magnetic resonance (<sup>1</sup>H NMR) and gas chromatography analyzer (GC). The Faraday efficiency (FE) of carbonaceous products (FE<sub>C-products</sub>) and liquid products (FE<sub>L-products</sub>) for these catalysts at various applied potentials were calculated (Fig. 4e and f), respectively. Notably, the FE<sub>C-products</sub> and FE<sub>L-products</sub> of N-CuSe-3 were 81.3% and 78.7% (at  $-1.1 \text{ V}$  vs. RHE), respectively, which were more than 2 and 5 folds as those catalyzed by the pristine CuSe (FE<sub>C-products</sub> of 39.8% and FE<sub>L-products</sub> of 15.4%).

We then analyzed the composition of the electro-reduced carbonaceous products by N-CuSe-3 at a potential range of  $-0.9 \text{ V}$  to  $-1.3 \text{ V}$ . The FE<sub>C-products</sub> of N-CuSe-3 (Fig. 4g) mainly contained CO (1.9%), formate (55.2%), acetate (8.9%), ethanol (14.6%) and H<sub>2</sub> (18.5%) at  $-1.1 \text{ V}$  vs. RHE. Remarkably, the yields of liquid products catalyzed by N-CuSe-3 (Fig. 4h) were rather high, including formate ( $\sim 22.1 \text{ mg h}^{-1} \text{ cm}^{-2}$ ), acetate ( $\sim 1.2 \text{ mg h}^{-1} \text{ cm}^{-2}$ ), and ethanol ( $\sim 1.0 \text{ mg h}^{-1} \text{ cm}^{-2}$ ), respectively. The eminent current density and yields of L-products of N-CuSe-3 are among the best records of all the electrocatalysts ever reported (Fig. S7). Moreover, as the reaction stability is crucial for electrocatalysts in real-time applications, 30-hours durability potentiostatic mapping on the partial current density and FE of N-CuSe-3 (Fig. 4i) were carried out at  $-1.1 \text{ V}$  vs. RHE. The results showed barely any decay in partial current density, together with a steady FE of more than 75% for

L-products containing more than 23% C<sub>2</sub> products (acetate and ethanol), further demonstrating the high electrocatalytic activity of N-CuSe-3. Aside from the steady performance, the well-maintained morphology and crystallization nature after 30 h reaction ascertained the good stability of N-CuSe-3 (Fig. S8).

### 3.4. CO<sub>2</sub>RR enhancement mechanisms

To figure out the crucial factors contributed to the electrocatalytic activity of N-CuSe-3, we evaluated its double layer capacitance ( $C_{dl}$ ) in a three-electrode system and determined the electrochemical surface area (ECSA) by measuring the curves of cyclic voltammetry (CV) at different scan rates (Fig. S9). As revealed in Fig. 5a, the  $C_{dl}$  increased from  $3.4 \text{ mF cm}^{-2}$  for the pristine CuSe to  $4.2 \text{ mF cm}^{-2}$  for N-CuSe-3. The normalized  $C_{dl}$  current density suggested that the electrocatalytic activity of N-CuSe-3 was not mainly contributed by the ECSA, but by the N injection, which induced higher electrocatalytic activity and current density for carbonaceous products (Fig. S10) [51]. By regulating the loading of catalysts on the working electrode, the linear relationship between  $C_{dl}$  and the normalized partially current density of liquid products ( $j_{L-normalized}$ ) was established (Fig. 5b), where the slope of linear fitting increased from  $4.0 \text{ mA mF}^{-1}$  for the pristine CuSe to  $10.6 \text{ mA mF}^{-1}$  for N-CuSe-3, further demonstrating the evident improvement induced by N injection on electrocatalytic CO<sub>2</sub>RR.

We then analyzed the rate-determining step during CO<sub>2</sub>RR. The Tafel slope (Figs. 5c and S11) was first plotted for the pristine CuSe and N-CuSe- $\alpha$  ( $\alpha = 1, 2, 3, 5$ ), deducing a value of  $101 \text{ mV dec}^{-1}$  for the pristine CuSe and around  $80 \text{ mV dec}^{-1}$  for the N-injected samples, which were close to the theoretical value for the CO<sub>2</sub> activation process ( $118 \text{ mV dec}^{-1}$ ) and surface reaction process ( $59 \text{ mV dec}^{-1}$ ), respectively [52]. In this regard, for the pristine CuSe, the CO<sub>2</sub> activation on the catalyst surface limited the CO<sub>2</sub> conversion efficiency; for N-CuSe- $\alpha$ , the rate-determining step switched to the process of electron transfer to activated CO<sub>2</sub> molecules. The N-CuSe-3 held the smallest slope value ( $78 \text{ mV dec}^{-1}$ ), corresponding the most effective CO<sub>2</sub>RR. The Nyquist plot (Fig. 5d) revealed that N injection led to improved conductivity hence more convenient charge transfer, benefiting electrocatalytic

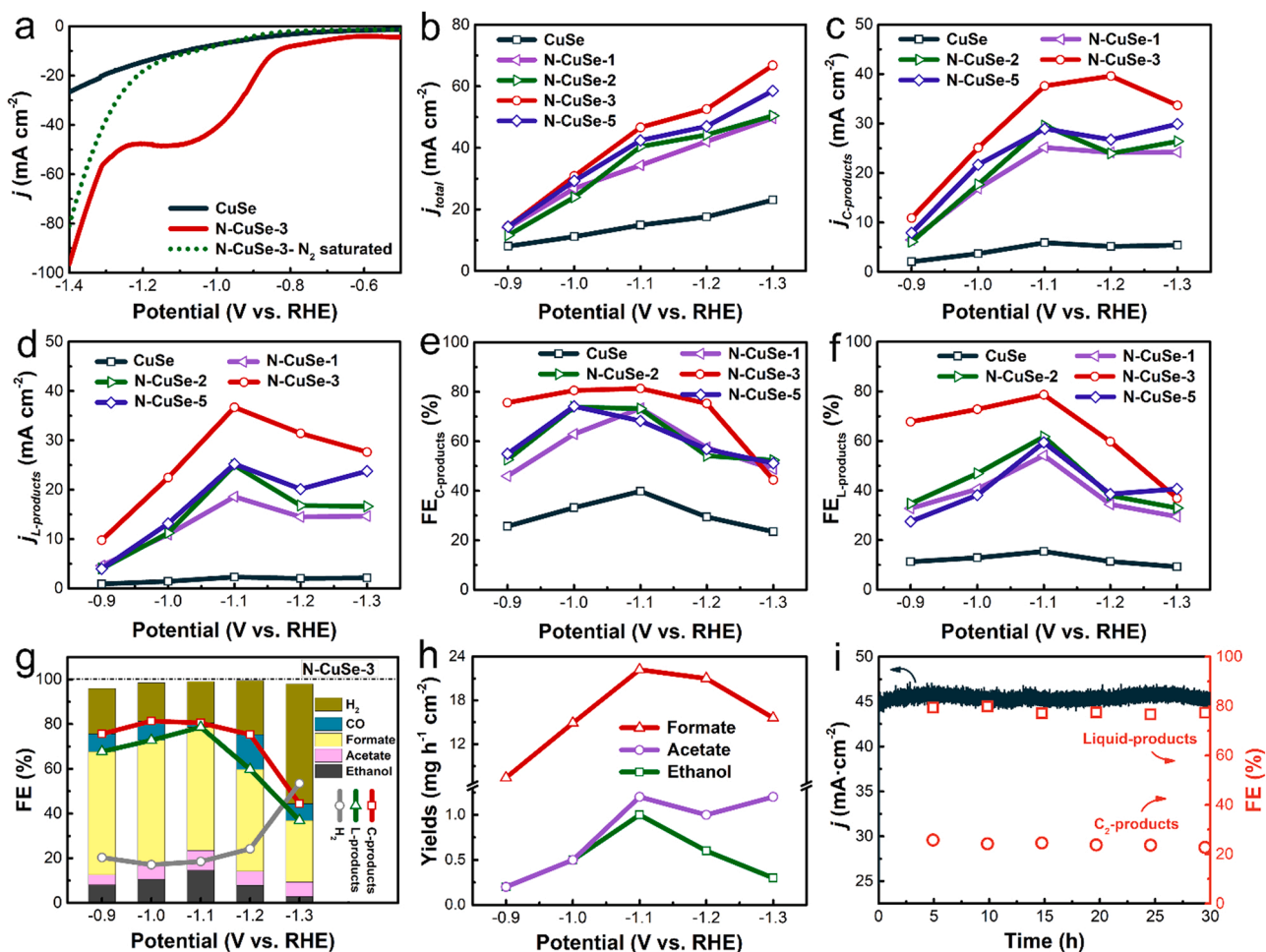


**Fig. 4.** Performance of CO<sub>2</sub> electrocatalytic reduction by the N-CuSe nanosheets. (a) The dynamic change of LSV curves for N-CuSe-3 and the pristine CuSe nanosheets in a CO<sub>2</sub>-saturated 0.5 mol L<sup>-1</sup> KHCO<sub>3</sub> and for N-CuSe-3 nanosheets in N<sub>2</sub>-saturated solution. (b) Geometrical current densities ( $j_{total}$ ), (c) partial current density for carbonaceous products ( $j_{C-products}$ ), and (d) partial current density for liquid products ( $j_{L-products}$ ) by N-CuSe- $\alpha$  ( $\alpha = 1, 2, 3, 5$ ) and the pristine CuSe. (e) Faradaic efficiency (FE) of carbonaceous products ( $FE_{C-products}$ ) and (f) FE of liquid products ( $FE_{L-products}$ ) by N-CuSe- $\alpha$  at various applied potentials. (g) The distribution of CO<sub>2</sub> reduced products and (h) the yields of formate, acetate, and ethanol catalyzed by N-CuSe-3 nanosheets at various applied potentials. (i) 30-hour potentiostatic mapping of  $j_{total}$  and FE for carbonaceous products catalyzed by N-CuSe-3 at  $-1.1$  V vs. RHE.

## CO<sub>2</sub>RR.

In addition, we carried out the electrochemical impedance spectroscopic analysis and used Mott-Schottky equation to verify the improved conductivity of the nanosheets. The linear relationship of  $1/C^2$  vs. various applied potentials (Figs. 5e and S12) showed a positive slope ( $dC^{-2}/dV$ ) for both the pristine and N-injected CuSe, suggesting that electrons were the main carriers in the present cases. As the slope was inversely proportional to the carrier density [53], the slope of the pristine CuSe nanosheets ( $3.67 \times 10^6 \text{ cm}^4 \text{ F}^{-2} \text{ V}^{-1}$ ) was higher than that of N-injected samples. The value of N-CuSe-3 ( $1.13 \times 10^6 \text{ cm}^4 \text{ F}^{-2} \text{ V}^{-1}$ ) was lowest among the samples, indicating its highest carrier density. Considering the binding intensity of catalyst surface with OH<sup>-</sup> was positively correlated to that with CO<sub>2</sub>, we conducted oxidative LSV scanning (Fig. 5f) to evaluate CO<sub>2</sub> activation in OH<sup>-</sup>-rich alkali electrolyte for the nanosheets [54]. The characteristic OH<sup>-</sup> absorption peak of N-CuSe-3 appeared at  $-0.03$  V, which was more negative than that of the pristine CuSe ( $0.04$  V), indicating the stronger OH<sup>-</sup> binding intensity hence higher CO<sub>2</sub> active ability in the case of N-CuSe-3, which benefit the CO<sub>2</sub> electrocatalytic reduction.

Based on these results, the simultaneous enhancement of conductivity, active sites and structural strain of N-CuSe have been also justified experimentally: (1) the increased current density (Fig. 4a) and reduced impedance (Fig. 5d and e) reveal the promoted metallic nature; (2) the

varied peak positions in XRD (Fig. 2f), Raman spectrum (Fig. 3d) and EXAFS spectrum (Fig. 3f) indicate the lattice distortion hence structural strain; (3) the promoted CO<sub>2</sub>RR performance (Fig. 5a and b), decreased Tafel slope (i.e. smaller overpotential and more complete reaction, Fig. 5c) and stronger adsorption for OH<sup>-</sup> (Fig. 5f) all suggest the formation of active sites. All these experimental results well support our theoretical prediction (Fig. 1). The abundant electrons accumulated around the N atoms hence favorable active sites, the enhanced surface carrier density and conductivity, and the promoted OH<sup>-</sup> binding intensity benefit the generation of carbonaceous products over H<sub>2</sub> in the electroreduction reaction, leading to high activity, yield and selectivity for CO<sub>2</sub>RR.

## 4. Conclusions

By one-step mild reaction with NH<sub>3</sub>, N atoms have been successfully injected in the cubic-phase ultrathin CuSe nanosheets (thickness of  $\sim 4.5$  nm). The N injection leads to significant variations: the DOS near the Fermi level increases and the bandgap disappears; the interlayer spacing of N-CuSe is enlarged with Cu and Se atoms slightly deviated from the original configuration; abundant electrons are accumulated around the N sites. Consequently, simultaneous enhancement of conductivity, active sites and structural strain is achieved, giving rise to

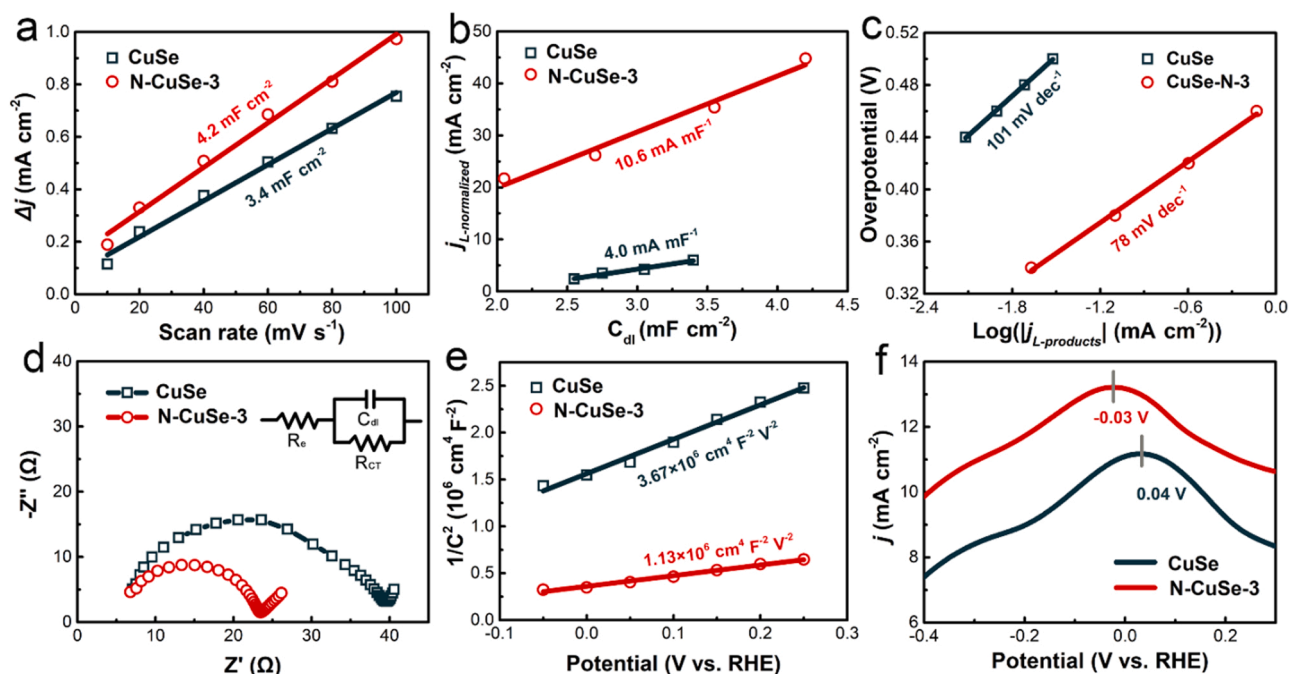


**Fig. 5.** Origin of the enhanced electrochemical properties for the N-CuSe nanosheets. (a) Charging current density differences plotted against scan rates, where the double layer capacitance ( $C_{dl}$ ) values can be deduced from the fitting slopes. The values of fitting slope are twice that of the  $C_{dl}$ . (b) Partial current density at  $-1.1 \text{ V}$  vs. RHE plotted against  $C_{dl}$ . (c) Tafel plots for liquid production, (d) Nyquist plots and (e) Mot-Schottky plots of N-CuSe-3 and the pristine CuSe. (f) The oxidative LSV scans for  $\text{OH}^-$  adsorption on N-CuSe-3 and the pristine CuSe in  $\text{N}_2$ -saturated  $0.1 \text{ mol L}^{-1}$  KOH electrolyte.

increased current density, reduced impedance, stronger adsorption upon  $\text{CO}_2$ , presence of  $\text{C}_2$  products, and boosted yield. As a result, the N-injected nanosheets delivers a high current density of  $46.7 \text{ mA cm}^{-2}$  at  $-1.1 \text{ V}$  vs. RHE (over 3-folds as that of the pristine CuSe) and a high yield of liquid products containing formate ( $\sim 22.1 \text{ mg h}^{-1} \text{ cm}^{-2}$ , over 11-folds as that of CuSe), acetate ( $\sim 1.2 \text{ mg h}^{-1} \text{ cm}^{-2}$ ), and ethanol ( $\sim 1.0 \text{ mg h}^{-1} \text{ cm}^{-2}$ ), respectively. The current density and yields of L-products are among the best records of all the electrocatalysts ever reported. In addition, the N-CuSe nanosheets show high chemical stability, with the high catalytic performance well-maintained for 10 h continuous operation. This work thus provides a facile and promising strategy to promote electrocatalysts by enhancing their conductivity, active sites and structural strain simultaneously for electrolytic fuel synthesis.

#### CRediT authorship contribution statement

**Yi Li:** Conceptualization, Investigation, Writing – original draft preparation. **Guoqiang Shi:** Calculation, Methodology. **Tao Chen:** Methodology, Characterization. **Lin Zhu:** Investigation, Validation. **Dengfeng Yu:** Investigation. **Ye Sun:** Writing – review & editing, Supervision, Funding acquisition. **Flemming Besenbacher:** Reviewing, Supervision. **Miao Yu:** Writing – review & editing, Supervision, Funding acquisition.

#### Declaration of Competing Interest

The authors declare that they have no known competing financial interests or personal relationships that could have appeared to influence the work reported in this paper.

#### Acknowledgments

This work is financially supported by the National Natural Science Foundation of China (51772066, 52073074, 21473045), and State Key Laboratory of Urban Water Resource and Environment, Harbin Institute of Technology (2021TS08).

#### Appendix A. Supporting information

Supplementary data associated with this article can be found in the online version at [doi:10.1016/j.apcatb.2022.121080](https://doi.org/10.1016/j.apcatb.2022.121080).

#### References

- [1] F. Pan, Y. Yang, Designing  $\text{CO}_2$  reduction electrode materials by morphology and interface engineering, *Energy Environ. Sci.* 13 (2020) 2275–2309.
- [2] J. Gu, C.-S. Hsu, L. Bai, H.M. Chen, X. Hu, Atomically dispersed  $\text{Fe}^{3+}$  sites catalyze efficient  $\text{CO}_2$  electroreduction to CO, *Science* 364 (2019) 1091–1094.
- [3] A. Vasileff, C. Xu, Y. Jiao, Y. Zheng, S.-Z. Qiao, Surface and interface engineering in copper-based bimetallic materials for selective  $\text{CO}_2$  electroreduction, *Chem* 4 (2018) 1809–1831.
- [4] G. Díaz-Sainz, M. Alvarez-Guerra, B. Ávila-Bolívar, J. Solla-Gullón, V. Montiel, A. Iribien, Improving trade-offs in the figures of merit of gas-phase single-pass continuous  $\text{CO}_2$  electrocatalytic reduction to formate, *Chem. Eng. J.* 405 (2021), 126965.
- [5] L. Zhang, Z.-J. Zhao, J. Gong, Nanostructured materials for heterogeneous electrocatalytic  $\text{CO}_2$  reduction and their related reaction mechanisms, *Angew. Chem. Int. Ed.* 56 (2017) 11326–11353.
- [6] Y. Wu, Z. Jiang, X. Lu, Y. Liang, H. Wang, Domino electroreduction of  $\text{CO}_2$  to methanol on a molecular catalyst, *Nature* 575 (2019) 639–642.
- [7] D. Voiry, H.S. Shin, K.P. Loh, M. Chhowalla, Low-dimensional catalysts for hydrogen evolution and  $\text{CO}_2$  reduction, *Nat. Rev. Chem.* 2 (1) (2018) 0105.
- [8] J. Li, R. Wei, X. Wang, Y. Zuo, X. Han, J. Arbiol, J. Llorca, Y. Yang, A. Cabot, C. Cui, Selective methanol-to-formate electrocatalytic conversion on branched nickel carbide, *Angew. Chem. Int. Ed.* 59 (47) (2020) 20826–20830.
- [9] F. Zeng, C. Mebrahtu, X. Xi, L. Liao, J. Ren, J. Xie, H.J. Heeres, R. Palkovits, Catalysts design for higher alcohols synthesis by  $\text{CO}_2$  hydrogenation: Trends and future perspectives, *Appl. Catal. B Environ.* 291 (2021).
- [10] C. Xie, Z. Niu, D. Kim, M. Li, P. Yang, Surface and interface control in nanoparticle catalysis, *Chem. Rev.* 120 (2020) 1184–1249.
- [11] H. Liu, Y. Zhu, J. Ma, Z. Zhang, W. Hu, Recent advances in atomic-level engineering of nanostructured catalysts for electrochemical  $\text{CO}_2$  reduction, *Adv. Funct. Mater.* 30 (2020), 1910534.
- [12] Y. Mun, K. Kim, S. Kim, S. Lee, S. Lee, S. Kim, W. Choi, S.-K. Kim, J.W. Han, J. Lee, A novel strategy to develop non-noble metal catalyst for  $\text{CO}_2$  electroreduction: Hybridization of metal-organic polymer, *Appl. Catal. B Environ.* 236 (2018) 154–161.
- [13] L. Wang, W. Zhang, X. Zheng, Y. Chen, W. Wu, J. Qiu, X. Zhao, X. Zhao, Y. Dai, J. Zeng, Incorporating nitrogen atoms into cobalt nanosheets as a strategy to boost catalytic activity toward  $\text{CO}_2$  hydrogenation, *Nat. Energy* 2 (2017) 869–876.

- [14] Z. Chen, T. Wang, B. Liu, D. Cheng, C. Hu, G. Zhang, W. Zhu, H. Wang, Z.-J. Zhao, J. Gong, Grain-boundary-rich copper for efficient solar-driven electrochemical CO<sub>2</sub> reduction to ethylene and ethanol, *J. Am. Chem. Soc.* 142 (2020) 6878–6883.
- [15] P. Zhang, W. Wang, H. Wang, Y. Li, C. Cui, Tuning hole accumulation of metal oxides promotes the oxygen evolution rate, *ACS Catal.* 10 (2020) 10427–10435.
- [16] D. Wu, G. Huo, W. Chen, X.-Z. Fu, J.-L. Luo, Boosting formate production at high current density from CO<sub>2</sub> electroreduction on defect-rich hierarchical mesoporous Bi/Bi<sub>2</sub>O<sub>3</sub> junction nanosheets, *Appl. Catal. B Environ.* 271 (2020), 118957.
- [17] X. Zhang, Z. Chen, M. Jiao, X. Ma, K. Mou, F. Cheng, Z. Wang, X. Zhang, L. Liu, Defects and conductive nitrogen-carbon framework regulated zninox nanosheets for boosting CO<sub>2</sub> electrocatalytic reduction, *Appl. Catal. B Environ.* 279 (2020), 119383.
- [18] F.P.G. de Arquer, D. Cao-Thang, A. Ozden, J. Wicks, C. McCallum, A.R. Kirmani, N. Dae-Hyun, C. Gabardo, A. Seifitokaldani, X. Wang, Y.C. Li, F. Li, J. Edwards, L. J. Richter, S.J. Thorpe, D. Sinton, E.H. Sargent, CO<sub>2</sub> electrolysis to multicarbon products at activities greater than 1 A cm<sup>-2</sup>, *Science* 367 (6478) (2020) 661–666.
- [19] G. Li, G.R. Blake, T.T.M. Palstra, Vacancies in functional materials for clean energy storage and harvesting: the perfect imperfection, *Chem. Soc. Rev.* 46 (2017) 1693–1706.
- [20] B. Li, T. Xing, M. Zhong, L. Huang, N. Lei, J. Zhang, J. Li, Z. Wei, A two-dimensional Fe-doped SnS<sub>2</sub> magnetic semiconductor, *Nat. Commun.* 8 (2017) 1958.
- [21] M. Acerce, D. Voiry, M. Chhowalla, Metallic 1T phase MoS<sub>2</sub> nanosheets as supercapacitor electrode materials, *Nat. Nanotechnol.* 10 (2015) 313–318.
- [22] X. Geng, W. Sun, W. Wu, B. Chen, A. Al-Hilo, M. Benamara, H. Zhu, F. Watanabe, J. Cui, T.-p. Chen, Pure and stable metallic phase molybdenum disulfide nanosheets for hydrogen evolution reaction, *Nat. Commun.* 7 (2016) 10672.
- [23] Z. Xia, S. Guo, Strain engineering of metal-based nanomaterials for energy electrocatalysis, *Chem. Soc. Rev.* 48 (2019) 3265–3278.
- [24] H. Huang, H. Jia, Z. Liu, P. Gao, J. Zhao, Z. Luo, J. Yang, J. Zeng, Understanding of strain effects in the electrochemical reduction of CO<sub>2</sub>: Using Pd nanostructures as an ideal platform, *Angew. Chem. Int. Ed.* 56 (2017) 3594–3598.
- [25] P. Strasser, S. Koh, T. Anniyev, J. Greeley, K. More, C. Yu, Z. Liu, S. Kaya, D. Nordlund, H. Ogasawara, M.F. Toney, A. Nilsson, Lattice-strain control of the activity in dealloyed core-shell fuel cell catalysts, *Nat. Chem.* 2 (2010) 454–460.
- [26] B. Hammer, J.K. Nørskov, Theoretical surface science and catalysis-calculations and concepts, *Adv. Catal.* 45 (2000) 71–129.
- [27] G. Kresse, J. Furthmüller, Efficient iterative schemes for ab initio total-energy calculations using a plane-wave basis set, *Phys. Rev. B* 54 (1996) 11169–11186.
- [28] G. Kresse, J. Hafner, Ab initio molecular dynamics for open-shell transition metals, *Phys. Rev. B* 48 (1993) 13115–13118.
- [29] J.P. Perdew, K. Burke, M. Ernzerhof, Perdew, Burke, and Ernzerhof of reply, *Phys. Rev. Lett.* 80 (1998), 891–891.
- [30] J. Xu, Q. Yang, W. Kang, X. Huang, C. Wu, L. Wang, L. Luo, W. Zhang, C.-S. Lee, Water evaporation induced conversion of CuSe nanoflakes to Cu<sub>2-x</sub>Se hierarchical columnar superstructures for high-performance solar cell applications, *Part. Part. Syst. Charact.* 32 (2015) 840–847.
- [31] P. Qiu, M.T. Agne, Y. Liu, Y. Zhu, H. Chen, T. Mao, J. Yang, W. Zhang, S.M. Haile, W.G. Zeier, J. Janek, C. Uher, X. Shi, L. Chen, G.J. Snyder, Suppression of atom motion and metal deposition in mixed ionic electronic conductors, *Nat. Commun.* 9 (2018) 2910.
- [32] P. Qiu, T. Mao, Z. Huang, X. Xia, J. Liao, M.T. Agne, M. Gu, Q. Zhang, D. Ren, S. Bai, X. Shi, G.J. Snyder, L. Chen, High-efficiency and stable thermoelectric module based on liquid-like materials, *Joule* 3 (2019) 1538–1548.
- [33] J. Masud, W.P.R. Liyanage, X. Cao, A. Saxena, M. Nath, Copper selenides as high-efficiency electrocatalysts for oxygen evolution reaction, *ACS Appl. Energy Mater.* 1 (2018) 4075–4083.
- [34] L.E. Marbella, X.Y. Gan, D.C. Kaseman, J.E. Millstone, Correlating carrier density and emergent plasmonic features in Cu<sub>2-x</sub>Se nanoparticles, *Nano Lett.* 17 (2017) 2414–2419.
- [35] D. Yang, Q. Zhu, C. Chen, H. Liu, Z. Liu, Z. Zhao, X. Zhang, S. Liu, B. Han, Selective electroreduction of carbon dioxide to methanol on copper selenide nanocatalysts, *Nat. Commun.* 10 (2019) 677.
- [36] K. Chan, C. Tsai, H.A. Hansen, J.K. Nørskov, Molybdenum sulfides and selenides as possible electrocatalysts for CO<sub>2</sub> reduction, *ChemCatChem* 6 (2014) 1899–1905.
- [37] A. Zhang, Y. Liang, H. Li, X. Zhao, Y. Chen, B. Zhang, W. Zhu, J. Zeng, Harmonizing the electronic structures of the adsorbate and catalysts for efficient CO<sub>2</sub> reduction, *Nano Lett.* 19 (2019) 6547–6553.
- [38] L. Ye, Y. Ying, D. Sun, Z. Zhang, L. Fei, Z. Wen, J. Qiao, H. Huang, Highly efficient porous carbon electrocatalyst with controllable N-species content for selective CO<sub>2</sub> reduction, *Angew. Chem. Int. Ed.* 59 (2020) 3244–3251.
- [39] P. Ravindran, P. Vajeeston, H. Fjellvåg, A. Kjekshus, Chemical-bonding and high-pressure studies on hydrogen-storage materials, *Comp. Mater. Sci.* 30 (2004) 349–357.
- [40] S. Livraghi, M.C. Paganini, E. Giamello, A. Selloni, C. Di Valentin, G. Pacchioni, Origin of photoactivity of nitrogen-doped titanium dioxide under visible light, *J. Am. Chem. Soc.* 128 (2006) 15666–15671.
- [41] X. Wang, X. Li, L. Zhang, Y. Yoon, P.K. Weber, H. Wang, J. Guo, H. Dai, N-doping of graphene through electrothermal reactions with ammonia, *Science* 324 (2009) 768–771.
- [42] B. Luo, J. Liu, H. Guo, X. Liu, R. Song, K. Shen, Z.M. Wang, D. Jing, G.S. Selopal, F. Rosei, High efficiency photoelectrochemical hydrogen generation using eco-friendly Cu doped Zn-In-Se colloidal quantum dots, *Nano Energy* 88 (2021), 106220.
- [43] Y. Qu, Z. Li, W. Chen, Y. Lin, T. Yuan, Z. Yang, C. Zhao, J. Wang, C. Zhao, X. Wang, F. Zhou, Z. Zhuang, Y. Wu, Y. Li, Direct transformation of bulk copper into copper single sites via emitting and trapping of atoms, *Nat. Catal.* 1 (2018) 781–786.
- [44] F. Li, M. Zhang, D. Benetti, L. Shi, L.V. Besteiro, H. Zhang, J. Liu, G.S. Selopal, S. Sun, Z. Wang, Q. Wei, F. Rosei, “Green”, gradient multi-shell CuInSe<sub>2</sub>/ (CuInSe<sub>2</sub>S<sub>1-x</sub>)<sub>5</sub>/CuInS<sub>2</sub> quantum dots for photo-electrochemical hydrogen generation, *Appl. Catal. B Environ.* 280 (2021), 119402.
- [45] R. Asahi, T. Morikawa, T. Ohwaki, K. Aoki, Y. Taga, Visible-light photocatalysis in nitrogen-doped titanium oxides, *Science* 293 (2001) 269–271.
- [46] J. Wang, D.N. Tafen, J.P. Lewis, Z. Hong, A. Manivannan, M. Zhi, M. Li, N. Wu, Origin of photocatalytic activity of nitrogen-doped TiO<sub>2</sub> nanobelts, *J. Am. Chem. Soc.* 131 (2009) 12290–12297.
- [47] I.G. Shitu, Z.A. Talib, J.L.Y. Chi, M.M.A. Kechick, H. Baqiah, Influence of tartaric acid concentration on structural and optical properties of CuSe nanoparticles synthesized via microwave assisted method, *Results Phys.* 17 (2020), 103041.
- [48] S. Schlücker, Surface-enhanced Raman spectroscopy: Concepts and chemical applications, *Angew. Chem. Int. Ed.* 53 (2014) 4756–4795.
- [49] Z. Jiang, T. Wang, J. Pei, H. Shang, D. Zhou, H. Li, J. Dong, Y. Wang, R. Cao, Z. Zhuang, W. Chen, D. Wang, J. Zhang, Y. Li, Discovery of main group single Sb-N<sub>4</sub> active sites for CO<sub>2</sub> electroreduction to formate with high efficiency, *Energy Environ. Sci.* 13 (2020) 2856–2863.
- [50] S. Gao, Z. Sun, W. Liu, X. Jiao, X. Zu, Q. Hu, Y. Sun, T. Yao, W. Zhang, S. Wei, Y. Xie, Atomic layer confined vacancies for atomic-level insights into carbon dioxide electroreduction, *Nat. Commun.* 8 (2017) 14503.
- [51] Z. Chen, T. Fan, Y.-Q. Zhang, J. Xiao, M. Gao, N. Duan, J. Zhang, J. Li, Q. Liu, X. Yi, J.-L. Luo, Wavy SnO<sub>2</sub> catalyzed simultaneous reinforcement of carbon dioxide adsorption and activation towards electrochemical conversion of CO<sub>2</sub> to HCOOH, *Appl. Catal. B Environ.* 261 (2020), 118243.
- [52] L. Wang, P. Liu, Y. Xu, Y. Zhao, N. Xue, X. Guo, L. Peng, Y. Zhu, M. Ding, Q. Wang, W. Ding, Enhanced catalytic activity and stability of bismuth nanosheets decorated by 3-aminopropyltriethoxysilane for efficient electrochemical reduction of CO<sub>2</sub>, *Appl. Catal. B Environ.* 298 (2021), 120602.
- [53] R. He, X. Yuan, P. Shao, T. Duan, W. Zhu, Hybridization of defective tin disulfide nanosheets and silver nanowires enables efficient electrochemical reduction of CO<sub>2</sub> into formate and syngas, *Small* 15 (2019), 1904882.
- [54] X. Yuan, Y. Luo, B. Zhang, C. Dong, J. Lei, F. Yi, T. Duan, W. Zhu, R. He, Decoration of In nanoparticles on In<sub>2</sub>S<sub>3</sub> nanosheets enables efficient electrochemical reduction of CO<sub>2</sub>, *Chem. Commun.* 56 (2020) 4212–4215.